

VLT/FORS1 spectrophotometry of the first planetary nebula discovered in the Phoenix dwarf galaxy

Ivo Saviane¹, Katrina Exter², Yiannis Tsamis³, Carmen Gallart⁴, and Daniel Péquignot^{5,*}

¹ ESO Chile, A. de Cordova 3107, Santiago e-mail: isaviane@eso.org

² STScI, 3700 San Martin Dr, Baltimore, MD 21218 USA e-mail: kexter@stsci.edu

³ Dept. of Physics and Astronomy, University College London, Gower Str., London, UK e-mail: ygt@star.ucl.ac.uk

⁴ IAC, c/ via Lactea s/n, La Laguna, Tenerife, Spain e-mail: carme@iac.es

⁵ LUTH, Observatoire de Paris, CNRS, Université Paris Diderot; 5 Place Jules Janssen, 92190 Meudon, France e-mail: Daniel.Pequignot@obspm.fr

Received xxx; accepted xxx

Abstract

Context. A planetary nebula (PN) candidate was discovered during FORS imaging of the Local Group dwarf galaxy Phoenix.

Aims. Use this PN to complement abundances from red-giant stars.

Methods. FORS spectroscopy was used to confirm the PN classification. Empirical methods and photoionization modelling were used to derive elemental abundances from the emission line fluxes and to characterize the central star.

Results. For the elements deemed most reliable for measuring the metallicity of the interstellar medium (ISM) from which the PN formed, $[O/H] \sim -0.46$ and $[Ar/H] \sim -1.03$. $[O/H]$ has lower measurement errors but greater uncertainties due to the unresolved issue of oxygen enrichment in the PN precursor star.

Conclusions. Earlier than 2 Gyr ago (the lower limit of the derived age for the central star) the ISM had $Z = 0.002-0.008$, a range slightly more metal-rich than the one provided by stars. Comparing our PN-to-stellar values to surveys for other dwarf Local Group galaxies, Phoenix appears as an outlier.

Key words. galaxies: dwarf – galaxies: individual: Phoenix – planetary nebulae: individual: PN Phoenix J01:51:05.46-44:26:55.28

1. Introduction

1.1. The Phoenix dwarf and its metallicity

Phoenix is a Local Group dwarf galaxy located 450 kpc from the Milky Way ($M_V = -10.1$, $L_V = 9 \times 10^5 L_\odot$, $M = 3.3 \times 10^6 M_\odot$, $(m - M)_0 = 23.2$; Mateo 1998). It has little current star formation (Martínez-Delgado, Gallart & Aparicio 1999, hereafter M99; Held, Saviane & Momany 1999, hereafter H99) and little or no H I gas (St-Germain et al. 1999; Gallart et al. 2001; Irwin & Tolstoy 2002; Young et al. 2007), which warrants its classification as a transition-type dwarf galaxy. From the color and width of the red-giant branch (RGB) one can infer quite a low metallicity for its intermediate-age and old stars: $[Fe/H] = -1.85$, $\sigma([Fe/H]) \approx 0.5$ dex (H99). However, metallicity estimates from the position of the RGB alone are quite uncertain in the case of composite stellar populations due to the resulting age-metallicity degeneracy (see, e.g. Pont et al. 2004). With a color-magnitude diagram (CMD) reaching the oldest main-sequence turnoffs, the RGB age-metallicity degeneracy may be partially broken since ages can be derived from the main-sequence, and $Z(t)$ can be estimated from the global fit of the distribution of stars in the CMD using stellar evolution models. In this way, Hidalgo, Aparicio & Martínez-Delgado-Delgado (2007; H07) have found that the current metallicity should be about $Z = 0.0015$.

In any case, spectroscopic data provide a more direct measurement of the metallicity and metallicity distribution of the stars in a galaxy. In the case of Phoenix, Ca II triplet spectra, which provide global metallicities, could be obtained for the brightest RGB stars in the galaxy. Measuring abundances directly, through high-resolution spectroscopy of individual stars, is not feasible due to the large distance of the galaxy. Moreover, there are no known H II regions, so the only other opportunity to obtain information on the abundances of particular elements is through a PN. During a FORS1 campaign (63.I-0642), a PN candidate was identified near the center of the galaxy, and in this paper we present our follow-up spectroscopy. The object was discovered due to its relative brightness in H α as compared with the V band, together with its star-like appearance (see Fig. 1). Following current convention we name this object PN Phoenix J01:51:05.45-44:26:55.28 but, in a light-hearted spirit, we choose to call it Bennu (the ancient Egyptian name for the phoenix).

1.2. Chemical abundances from PNe

PNe are the post-AGB (asymptotic giant branch) stage of low-to intermediate-mass stars. Their chemical abundances are those of the envelope of the precursor AGB star which was ejected via a stellar wind. The composition of the nebulae are a mixture of elements affected by the preceding nucleosynthesis and dredge-up cycles (e.g. He, C, and N) and elements unadulterated by stellar evolution (e.g. Ar, S, and in most cases also O and Ne). Measuring PN abundances is useful since they complement

Send offprint requests to: I. Saviane

* Based on data collected at the European Southern Observatory, VLT, Chile, Proposal N. 076.D-0089(A)

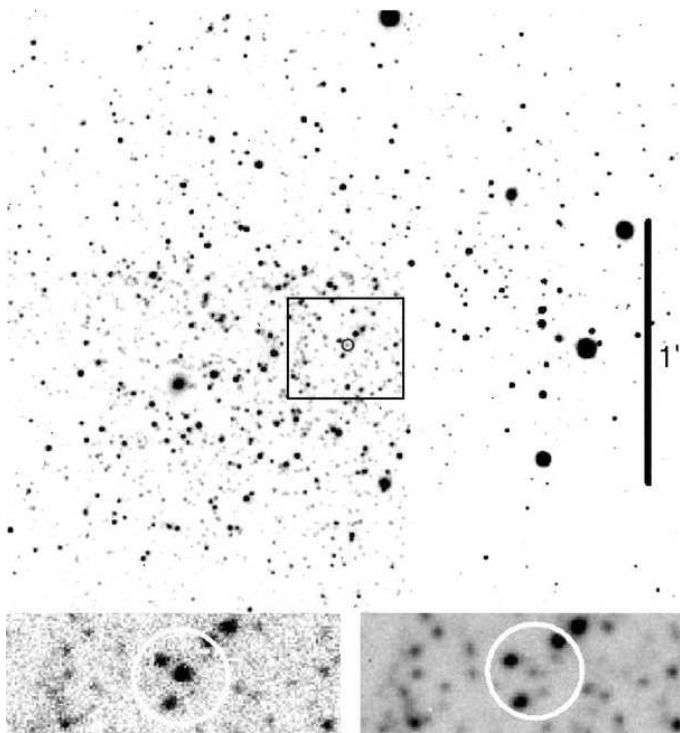


Figure 1. Finding chart for the Phoenix planetary nebula, obtained from FORS1 V-band imaging. The lower two insets show the appearance of the nebula in the $H\alpha$ band (left) and V band (right). North is up and east is to the left.

abundance determinations from stars, and contribute to the study of galactic chemical evolution (e.g., Shields 2002). For Phoenix, obtaining PN abundances is especially important, as this is one of the most metal poor Local Group galaxies. While with only one PN we are dealing with low number statistics, we note that the scatter about the mean oxygen abundance for PNe (the most often considered element in PN–galactic evolution studies) in other galaxies is usually less than a factor of two (Stasińska & Izotov 2003). Lacking any other determination, a sole PN can still provide crucial information.

2. Observations and data reduction

The spectroscopic observations were carried out in service mode on the night of November 26, 2005. The target can be identified in Fig. 1, which shows part of one FORS2 frame taken in the V band. Three FORS1 spectra of 1730 s each were taken, with the spectrograph in long-slit mode, a $0''.7$ slit, and with grism 300V+10. No order sorting filter was used, in order to have a higher throughput in the blue part of the spectrum, and the response function was then determined by observing a blue standard star in the same configuration. Some second-order contamination is expected at $\lambda > 6600 \text{ \AA}$, but it is less than 4% for the $[S II]$ lines at 6725 \AA . The nebula was observed at an airmass ~ 1.04 and under a seeing of $\sim 1''$, while approaching and crossing the meridian. During the evening twilight, the DA spectrophotometric standard EG21 from Hamuy et al. (1994) was observed. The instrument mode was slightly different than the one used for the science target: a $5''$ slit was created by placing the 19 movable slits of the MOS mode side by side, and aligning them along the parallactic angle; moreover, only the central part of the CCD was read out. The science data were instead

taken with one of the fixed-width slit masks, and the full CCD was read out. The two sets of calibration frames (biases, arc, and flat-fields) for the two configurations were taken in the morning following the observations.

Reductions were carried out using a customized version of the EFOSC2 quick-look tool¹, which is based on the ESO-MIDAS data reduction system. The usual bias subtraction and flat-fielding (from quartz lamps) were performed. He+HgCd+Ar arc frames were used to compute the 2-D wavelength calibration. The spectra were then linearly rebinned with a constant step of $\Delta\lambda = 2.64 \text{ \AA}$, with a resulting wavelength coverage of $3707\text{--}8289 \text{ \AA}$ at a resolution of $\sim 8.2 \text{ \AA}$ FWHM.

The two-dimensional sky frame was created by first sampling the sky spectrum in two windows flanking the target spectrum, and then fitting the spatial gradient with a one-degree polynomial. After sky-subtracting, the extraction window for the emission-line spectrum was chosen based on the spatial profile of the $H\alpha$ line, adjusting in order to reach an optimum signal-to-noise ratio (SNR). The flux of the spectrophotometric standard star was instead summed over almost the entire spatial profile, leaving out just the two sky windows. To compute the response function, the instrumental spectrum was corrected for atmospheric extinction, divided by the exposure time, and then divided by the published spectrum, and the ratio was fit with a 12th degree polynomial. Note that the different instrument setup of the standard does not affect the response function, which can therefore be applied to the science spectra. The three pre-processed, wavelength-calibrated, sky-subtracted and extracted spectra of the PN were flux-calibrated using this response function. Finally, the fiducial PN spectrum was obtained as a median of the three individual exposures, and it is shown in Fig. 2. The typical SNR measured on the continuum is five or better, while the $[O III] \lambda 4363$ line was detected with a SNR of ~ 24 . The continuum is due in part to the nebula and in part to the unresolved light of the Phoenix stellar population. Photoionization models (see below) predict that 39% of the observed continuum intensity at 5000 \AA is due to the nebula. Because of the low counts, no absorption lines can be detected, and no slope is visible.

3. Spectral measurements

Emission line fluxes and centroids were measured with the ELF Gaussian fitting routines of DIPSO (Howarth et al. 1998) and independently checked with the fitting routines of the MIDAS package. The FWHM for faint lines were fixed from near-by bright lines and were a free parameter for unresolved blends. The fluxes are reported in Table 1. The measured blended $H\beta$ +He II flux is $1.98 \times 10^{-16} \text{ erg cm}^{-2} \text{ s}^{-1}$ and the adopted de-reddened and de-blended $H\beta$ intensity² is $3.50 \times 10^{-16} \text{ erg cm}^{-2} \text{ s}^{-1}$. This value, which is used in the models of Section 4.2, incorporates a correction of +28% as the employed slit had a width of $0''.7$ and the PN was observed under $\sim 1''$ seeing.

The continuum in the very blue and red is fairly noisy, and a conservative approach was taken to deciding between a true line and a noise spike. This is especially important for the He I lines – because of the dependence of the calculated oxygen abundance on the helium abundances when using the ‘ICF’ method (see below) – and the $[S II]$ ratio, which is used to calculate the electron density. The sky is noisy in the $[S II]$ region, and the

¹ <http://www.ls.eso.org/>

² Correction for the He II contribution is calculated from theoretical He II line ratios to the uncontaminated He II 4686 \AA flux.

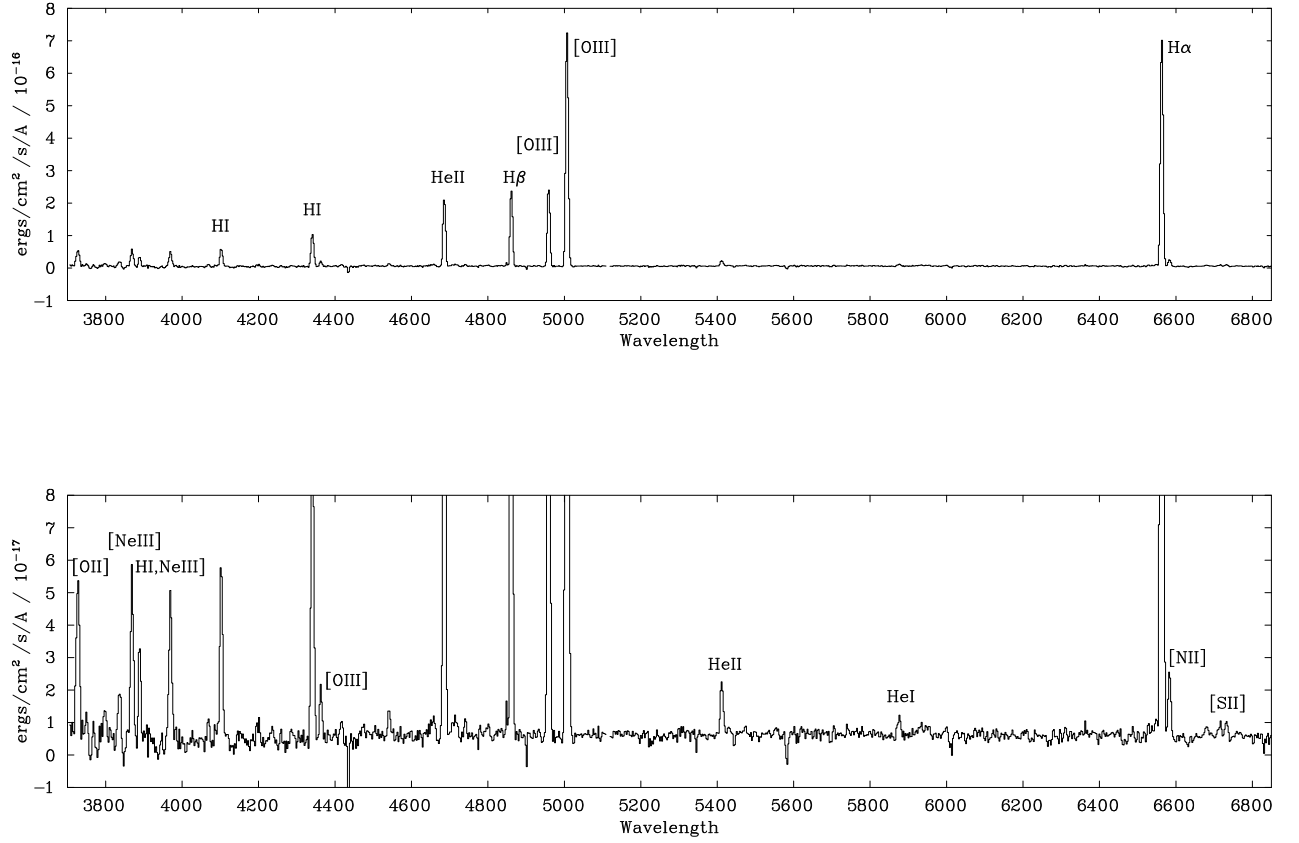


Figure 2. The calibrated and sky-subtracted spectrum of Benu, above, and again below, scaled to highlight the fainter lines.

[S II] fluxes very low. To estimate the effect this has on the measurement of the [S II] ratio we performed a sky subtraction in the standard manner (using the sky spectrum extracted from the slit and resulting in the fluxes quoted in Table 1) and a sky subtraction using rather a polynomial fit to the sky in this spectral region. The [S II] ratio from the poly-fit result is up to 70 % greater than that from the true-sky subtraction. Regarding He^+ , only the $\text{He I } \lambda 5876$ line, de-blended from $\text{He II } \lambda 5869.02$ (5–29), is considered in our analysis as the 4471 \AA and 6678 \AA lines are upper limit detections.

The $\text{H}\alpha/\text{H}\beta$ Balmer line ratio was used to calculate the extinction constant, yielding a value of $c(\text{H}\beta)=0.16$. The He II Pickering series is a contaminant of the H I lines in high excitation nebulae such as this one and their contribution was estimated via their theoretical ratios to $\text{He II } \lambda 4686$ following Storey & Hummer (1995); 13.5% of the $\lambda 4686$ flux at $\text{H}\alpha$ is due to $\text{He II } \text{Pi}$ (4–6) and 5.1 per cent at $\text{H}\beta$ is due to Pi (4–8), under case B conditions. The intrinsic value of the H I ratio to compare to when computing $c(\text{H}\beta)$ depends on the electron temperature, T_e , and density, n_e ; we iterated once between determining T_e and n_e before computing $c(\text{H}\beta)$. As the $\text{He II } \lambda \lambda 4541.59, 5411.53$ lines are well detected, we also computed, to compare, the reddening using the $\text{He II } \lambda 4686/\lambda 5411$ and $\lambda 5411/\lambda 4542$ ratios; this yielded a weighted average of $0.19 \pm 50\%$. We adopted the H I Balmer value to deredden the observed line fluxes, and used the Galactic extinction law of Howarth (1983).

A 16% correction has been applied to the $[\text{O II}] \lambda 3727$ doublet which is blended with the $\text{H } 14 \lambda 3721.9$, $[\text{S III}] \lambda 3721.6$ and $\text{H } 13 \lambda 3734.4$ lines: the $[\text{S III}] \lambda 3721$ flux was estimated from a comparison with the de-reddened flux of $[\text{S III}] \lambda 6312.1$, which originates from the same upper level. The latter line is blended with $\text{He II } \lambda 6310.8$ (5–16) in high excitation PNe and that flux was retrieved via its theoretical ratio relative to $\text{He II } \lambda 4686$. The $I(\text{H } 13)/I(\text{H}\beta)$ and $I(\text{H } 14)/I(\text{H}\beta)$ intensity ratios were estimated using theoretical H I line emissivities as above.

In Table 1 suggested ion identifications are given. The bluest H I line ratios, at $\lambda \leq 3968$, are a factor of 1.3–1.8 in excess of that expected theoretically, suggesting that the adopted blue continuum, possibly affected by interstellar absorption lines, is too low. $\text{H I } \lambda 3771$ is not detected in the spectrum.

4. Chemical abundances and central star parameters

4.1. Empirical analysis

A determination of chemical abundances was first carried out using the semi-empirical ICF (ionization correction factor) scheme reported in Kingsburgh & Barlow (1994). The abundances of each observed ionic species relative to H^+ are added up and multiplied by their corresponding ICF to yield elemental abundances relative to hydrogen. Input values in these calculations are the plasma T_e and n_e , whose values were computed from the

Table 1. Observed line fluxes.

$\lambda(\text{\AA})$	$F(\lambda)^a$	$I(\lambda)^b$	Err.(%)	ID
3727	54.1	26.83	10	[O II]
3749	10.4	5.73	50	H I
3798	13.4	7.37	30	H I
3836	18.6	10.20	15	H I
3869	48.6	28.05	10	[Ne III]
3889	24.5	13.54	10	H I, He I
3969	48.5	26.93	10	H I, [Ne III]
4069	6.43	3.66	25	[S II] ⁺ ^c
4102	51.4	27.75	10	H I
4341	95.1	50.43	10	H I
4363	15.0	8.32	10	[O III]
4541	7.46	4.07	40	He II
4657	5.59	3.02	50	C IV, [Fe III]
4686	182.	98.06	10	He II
4714	10.1	5.44	30	[Ar IV] ⁺ ^c
4740	5.06	2.71	35	[Ar IV]
4861	198.	100	10	H I
4959	210.	110	5	[O III]
5007	651.	341	5	[O III]
5412	17.2	8.68	20	He II
5876	5.70	2.77	30	He I
6312	3.11	1.11	50	[S III]
6563	630.	284	5	H I
6583	19.9	9.37	15	[N II]
6717	3.57	1.67	50	[S II]
6731	5.61	2.62	50	[S II]
7136	5.95	2.73	25	[Ar III]

[^a] In units of $10^{-18} \text{ erg cm}^{-2} \text{ s}^{-1}$.

[^b] De-reddened and ratioed to $H\beta = 100$. All H I lines de-blended from He II; [O II] 3727 de-blended from [S III] and two H I lines.

[^c] Blends: [S II] 4069 + [Fe V] 4071 + C III 4069; [Ar IV] 4711 + He I 4713 + [Ne IV] 4714+16.

Table 2. Empirical ionic abundances^a and ICF values for two electron densities.

Ion	500	3700	Ion	500	3700
[O II]	17.1	25.7	[S II]	0.38	0.54
[O III]	280.	279.	[S III]	3.87	4.30
icf(O)	3.96	3.96	icf(S)	1.82	1.61
[N II]	5.42	5.62	[Ar III]	0.93	0.93
icf(N)	73.1	50.0	[Ar IV]	1.82	1.64
[Ne III]	57.4	57.4	icf(Ar)	1.01	1.02
icf(Ne)	4.18	4.30			

[^a] In 10^{-7} by number relative to H.

de-reddened [O III] $\lambda 4363/(\lambda 5007 + \lambda 4959)$ and [S II] $\lambda 6717/6731$ ratios respectively.

The same atomic data references as in Exter et al. (2004) were used, with the exception of using helium where effective recombination coefficients were taken from Smits (1996) for Case B and adopting corrections for collisional excitation contributions as in Benjamin, Skillman and Smits (1999).

For the density measured from the [S II] ratio: to show the effect that measurement uncertainties (in particular, sky subtraction) has on the derived density we carried out here calculations using the [S II] ratio measured from the two sky-subtraction methods mentioned in Sec. 3. A higher density comes from the

Table 3. Abundances of Bennu vs solar^a

Element	$n_e = 500$	$= 3700$	Model	Sun
He/H	.125(20)	.125(20)	.108(10)	.098
O/H $\times 10^4$	1.18(14)	1.21(17)	1.7(13)	4.9
N/O $\times 10$	3.4(24)	2.3(26)	1.5(15)	1.6
Ne/O $\times 10$	2.0(30)	2.0(26)	1.4(15)	1.8
S/O $\times 10^3$	6.5(50)	6.5(50)	10. ^b	37.
Ar/O $\times 10^3$	2.4(30)	2.2(30)	2.3(25)	8.5

[^a] Proto-solar abundances from Asplund et al. (2005), except for O/H from Allende-Prieto et al. (2001). Percentage errors in parenthesis.

[^b] S/Ar solar; S/O $\times 10^3$ may as well be 20 according to model outputs.

lower ratio (from the fluxes we adopted and list in Table 1) and a lower density from the higher ratio. The effect on the Te value is minor, $T_e = 16\,600 \pm 1000 \text{ K}$, while n_e changes from 500 to 3700 cm^{-3} . In Tables 2 and 3 we give the ionic and total abundances with this range of n_e and T_e values. The percentage 1σ errors given in parenthesis in Table 3 include the flux and T_e measurement errors and not those inherent to the empirical methods (see Exter et al. 2004). In Table 3, errors for the model abundances (see Sect. 4.2) correspond either to the scatter among several model fits or to the flux errors.

Since the He II flux is very high, the nebula cannot be radiation bounded. Then the formulation of Kaler & Jacoby (1989) for estimating the T_{eff} of the central star only provides an upper limit to T_{eff} ($< 322 \text{ kK}$) and the one of Zijlstra & Pottasch (1989) a lower limit to L_{bol} ($> 270 L_{\odot}$). The method of Zanstra (1927) to obtain a T_{eff} (He II) requires knowledge of the stellar continuum (see below), while the energy balance method of Stoy (1933) requires knowledge of important gas coolants outside the optical range. Self-consistent photoionization modelling based on the optical line spectrum is the only available method for the determination of T_{eff} and L_{bol} .

4.2. Photoionization modelling

Photoionization models were computed with the code NEBU (e.g., Péquignot and Tsamis 2005), which was also used in a comprehensive study of the Sagittarius dwarf galaxy PN population (Dudziak et al. 2000; Péquignot et al. 2000; Zijlstra et al. 2006). Computations were done assuming that both the gas filling factor and the covering factor (solid angle as seen from the central star) were unity. The actual geometry of the nebula is not known due to lack of imaging and the inner radius R_{in} is a first free parameter. A two-sector model is suggested by the coexistence of a very strong He II $\lambda 4686$ line with [O II] and [S II] lines which implies that even though the nebula is strongly matter-bounded along most radial directions, some directions must be radiation-bounded to a large degree (One-sector models are however considered in Appendix A). The premise of two-sector models comprising both optically thick and thin components (advocated by, e.g., Clegg et al. 1987 in their analysis of the typical Galactic PN NGC 3918) is a realistic one, given that the majority of nearby spatially-resolved PNe are replete with optically thick inhomogeneities in the form of clumps/filaments/torii embedded in a more tenuous medium. The [S II] doublet ratio can be used to constrain the density or, more conveniently, the thermal pressure P_{out} of the (peripheral) thick clumps. The [Ar IV] doublet ratio is neither suitably accurate nor sensitive enough to n_e to constrain the inner high-ionization region density, $N_{\text{in}}(\text{H})$ (equiva-

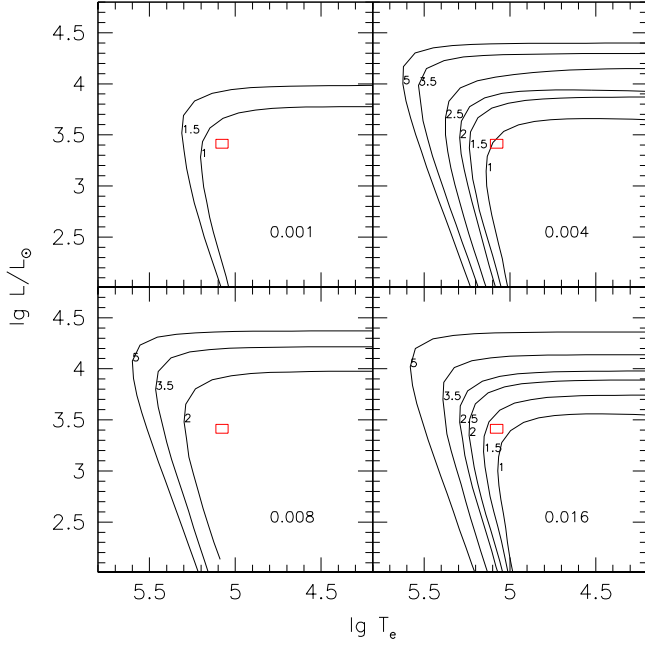


Figure 3. The theoretical, H-burning WD tracks from VW94 are represented here in the $\log L/L_\odot$ vs. $\log T_e$ plane. The four panels show four different metallicities, identified by the label, and for each metallicity tracks of different initial mass are plotted. A label near the knee of each track identifies its initial mass, in solar units. The open box represents the permitted range for the central star of Bennu, with parameters determined via photoionization modeling of the nebula.

lently, P_{in}), which is therefore a second free parameter. Adopting a sufficiently flexible description for the gas distribution allows the exploration of a realistically large space of solutions. In practice, the pair of (T_e, n_e) is obtained at each point by solving iteratively the statistical balance equations, assuming a variable gas pressure, P , given here as a function of the radial optical depth, τ , at 13.6 eV:

$$P(\tau) = \frac{P_{\text{out}} + P_{\text{in}}}{2} + \frac{P_{\text{out}} - P_{\text{in}}}{\pi} \tan^{-1} \left[\kappa \log \left(\frac{\tau}{\tau_c} \right) \right]. \quad (1)$$

At the first step of the computation ($\tau = 0$) the pressure is P_{in} , while at the last step ($\tau = \infty$; in practice $\gg 1$) it is P_{out} . The requirement for a sector (Sector 2) comprising radiation-bounded clumps immersed in a dilute medium dictates that $P_{\text{in}} < P_{\text{out}}$. The third parameter τ_c at which $P(\tau_c) = (P_{\text{in}} + P_{\text{out}})/2$ corresponds to the inner boundary of the generic clump. The fixed fourth parameter, $\kappa = 30$, is large enough to ensure a sharp clump boundary. For consistency, the optical depth τ_1 of the dilute matter-bounded Sector 1 must be substantially less than τ_c (in practice the condition $\tau_c/\tau_1 \geq 1.2$ was adopted).

The ionizing spectrum is described as a black body of temperature T_{BB} and luminosity L . According to stellar atmosphere models for hot stars, the ‘colour temperature’ of the bulk of the photoionizing continuum (the best equivalent black-body temperature) is larger than the actual effective temperature T_{eff} . When black-body spectra are used instead of genuine stellar atmosphere models in computing photoionization models, a recommended rough correction, adopted here, is:

$$T_{\text{eff}} = T_{\text{BB}} - 15 \text{ kK}. \quad (2)$$

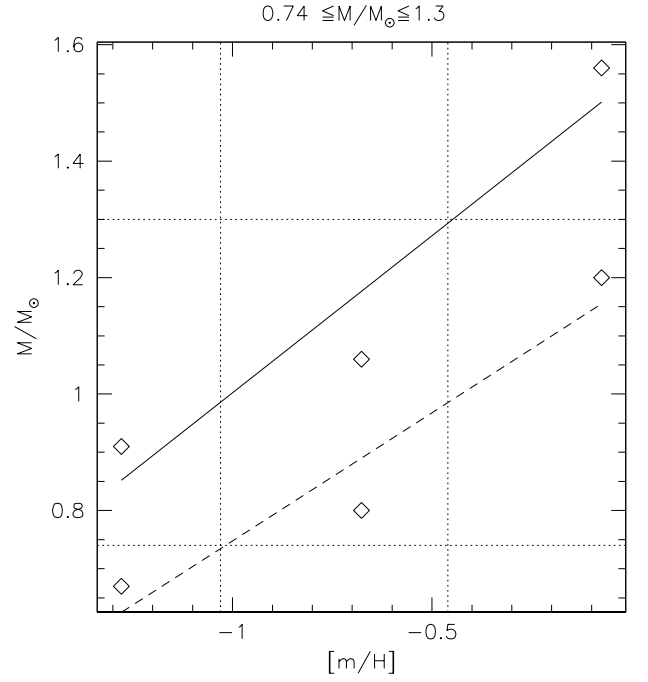


Figure 4. The dependence of the progenitor mass on the metallicity of the best-fitting WD track is illustrated by this plot. The lines are least-square fits to the discrete points corresponding to **three** of the four metallicities available in VW94 tracks (see Fig. 3). The fits have been repeated for the two combinations of $(T_e - \Delta T_e; L - \Delta L)$ (dashed line) and $(T_e + \Delta T_e; L + \Delta L)$ (solid line) allowed by our error estimates. The vertical dotted lines show the permitted metallicity range determined from the nebular emission lines, and the horizontal dotted lines mark the limits of the permitted progenitor mass.

Table 4. Constraints on model parameters.

Parameter	Constraint
R_{in}	free
$N_{\text{in}}(\text{H})$	free
T_{BB}	free
$\tau_1(\text{thin})$	absolute flux $I(\text{H}\beta)$
$f_2^{\text{cov}}(\text{thick})$	$[\text{O II}] \lambda 3727; (f_1^{\text{cov}} + f_2^{\text{cov}} = 1)$
P_{out}	ratio $[\text{S II}] \lambda 6731/\lambda 6716$
τ_c/τ_1	$\text{He I } \lambda 5876$ (see text)
L	ratio $[\text{Ar IV}] \lambda 4740 / [\text{Ar III}] \lambda 7135$
He	$\text{He II } \lambda 4686$
C	ratio $[\text{O III}] \lambda 4363/(\lambda 4959 + \lambda 5007)$
N	$[\text{N II}] \lambda 6584$
O	$[\text{O III}] \lambda 5007 + \lambda 4959$
Ne	$[\text{Ne III}] \lambda 3869$
S	$\text{S/Ar} = 4.37$ by number (solar); ‘ $[\text{S III}] \lambda 6312$ ’
Ar	$[\text{Ar III}] \lambda 7135 + [\text{Ar IV}] \lambda 4740$
Fe	$\text{Fe/H} = 4 \times 10^{-7}$ by number; ‘upper limit $[\text{Fe VI}]$ ’

(see, e.g., Dudziak et al. 2000).

The model parameters and corresponding dominant observational and technical constraints are listed in Table 4. Some potential constraints which were dismissed on account of the large uncertainties they entail are given in inverted commas. Thus, we assumed that S/Ar was solar (4.37 by number; Lodders 2003).

Table 5. Range of model parameters for ‘exact’ solutions

Parameter	1- σ box				
R_{in} (10^{17} cm)	1.0	1.0	1.0	1.4	–
$N_{\text{in}}(\text{H})$ (cm^{-3})	900	1200	1600	1200	–
T_{BB} (kK)	127 \pm 5	135 \pm 7	145 \pm 3	135 \pm 7	135 \pm 10
T_{eff} (kK)	112 \pm 5	120 \pm 7	130 \pm 3	120 \pm 7	120 \pm 10
L (10^{36} erg s $^{-1}$)	11. \pm 1	10. \pm 1	9. \pm 1	11. \pm 1	10. \pm 1
He/H $\times 10^3$	108 \pm 0	108 \pm 0	109 \pm 1	108 \pm 0	108 \pm 1
C/H $\times 10^6$	197 \pm 1	212 \pm 4	230 \pm 4	222 \pm 4	214 \pm 17
O/H $\times 10^6$	165 \pm 7	172 \pm 9	178 \pm 4	169 \pm 9	170 \pm 12
N/O $\times 10^3$	149 \pm 4	147 \pm 1	150 \pm 1	147 \pm 1	149 \pm 3
Ne/O $\times 10^3$	142 \pm 3	143 \pm 1	153 \pm 2	149 \pm 1	145 \pm 5
Ar/O $\times 10^5$	232 \pm 6	228 \pm 5	226 \pm 2	228 \pm 5	230 \pm 7

Also, no iron lines were detected and Fe/H was given a constant arbitrary value. There are 11 (+2 implicit for S and Fe) spectroscopic constraints controlling as many model parameters, leaving T_{BB} as a third free parameter, in addition to R_{in} and $N_{\text{in}}(\text{H})$ (see above). Gas cooling is dominated by carbon and oxygen line emission. For lack of measured carbon lines (no UV coverage), the carbon abundance is constrained by the energy balance through the [O III] ratio temperature. Given the three free parameters and assuming that all other constraints are systematically fulfilled, for increasing L , the computed [Ar IV]/[Ar III] increases and He I decreases moderately, while, for increasing τ_c/τ_1 , [Ar IV]/[Ar III] increases slowly and He I decreases again, until a limit is reached asymptotically for $\tau_c/\tau_1 > 2.5$ –3. Thus L and τ_c/τ_1 are primarily controlled by the ionization balances of argon and helium respectively. Other correspondences between parameters and constraints in Table 4 are straightforward.

The domain of ‘exact’ solutions according to the criteria listed in Table 4 has been scanned. Many iterations were needed to fulfill all constraints simultaneously and not all combinations of the 3 free parameters led to a solution. Results are summarized in Table 5. Given $R_{\text{in}} = 1 \times 10^{17}$ cm (our ‘standard’ value), the full range of T_{BB} leading to a solution was determined for the 3 given values of $N_{\text{in}}(\text{H})$ (cm^{-3}) = 900 ($P_{\text{out}}/P_{\text{in}} = 1.35$), 1200 (standard, $P_{\text{out}}/P_{\text{in}} = 1.95$), and 1600 ($P_{\text{out}}/P_{\text{in}} = 2.4$). The ratio [Ar IV]/[Ar III] being accounted for (correct choice of L), a minimum T_{BB} is obtained when He I happens to be computed too large and a maximum T_{BB} is obtained when τ_c/τ_1 decreases down to 1.2. After several trials, the resulting accessible domain on the (T_{BB} /kK, $L/10^{36}$ erg s $^{-1}$) plane was found to be an elongated ellipse, whose long-axis boundaries were at (120, 11.3) and (150, 8.7) respectively for $N_{\text{in}}(\text{H}) \sim 800$ (the minimum value since $P_{\text{out}}/P_{\text{in}} \sim 1.2$), and $\sim 1700 \text{ cm}^{-3}$: the larger the $N_{\text{in}}(\text{H})$, the more compact the nebula and the smaller the corresponding L are. Thus, for a given R_{in} , L correlates inversely with T_{BB} . The ‘1 σ box’ for the standard case, not including observational uncertainties, is T_{BB} /kK = 135 \pm 10 and $L/10^{36}$ erg s $^{-1}$ = 10 \pm 1. For $N_{\text{in}}(\text{H}) = 1200$, ‘exact’ models with $R_{\text{in}}/10^{17}$ cm = 1.4 instead of 1.0 were also obtained for a few T_{BB} ’s, showing that derived parameter values were about similar to those obtained previously, except for a 10% upward shift of L (Col. 5, Table 5). Conversely, for $R_{\text{in}}/10^{17}$ cm < 1.0, the previous solutions for standard R_{in} essentially apply. Model outputs are displayed in Table A.1 of Appendix A, including one solution (D135, Col. 3) belonging to the domain of most favorable values of model parameters (Table 5) and examples of models which are in some way unsatisfactory, including one-sector models. A more thorough discussion of the uncertainties is also given in Appendix B.

Model elemental abundances are relatively stable within the domain of ‘exact’ solutions (Col. 6, Table 5). Model outputs (see Col. 3 of Table A.1) suggest that any value of S/Ar between solar (adopted) and twice solar is possible. For higher T_{eff} ’s, O/H can be somewhat larger and Ar/O slightly smaller (Col. 4, Table A.1).

4.3. Parent star

For the central star, in the previous section we obtained best values $T_{\text{eff}} = 120 \pm 10$ kK and $L_{\text{bol}} = 2600 \pm 260 L_{\odot}$. To determine an age and mass for Bennu we have compared these model estimates to the H-burning white-dwarf (or PN central star) evolutionary tracks of Vassiliadis & Wood (1994; VW94), as shown by Fig. 3. As the metallicity increases, the progenitor mass of the best-fitting track increases. To have a quantitative estimate, for each metallicity the tracks were interpolated at the ($\log T_{\text{eff}}$, $\log L$) position of the WD, thus obtaining a mass-metallicity relation, which is shown in Fig. 4. Due to the small number of tracks and the large extrapolation from the PN location to any of them, the $Z = 0.008$ point was omitted from the fit. The procedure was repeated for the two extremes of the ($\log T_{\text{eff}}$; $\log L$) combinations allowed by the errors on the two quantities. By fitting the discrete points with linear regressions, one has continuous mass-metallicity relations, so entering with a metallicity value an estimate of the progenitor mass can be obtained. If we adopt the widest metallicity range discussed below ([m/H] = -1.03 from [Ar/H] to [m/H] = -0.46 from [O/H]), then the range of progenitor mass is between 0.74 and 1.30 M_{\odot} .

This low mass chimes well with the N/O ratio and He/H nebular abundance, both being sufficiently low to indicate a non-Type I, low central star mass status (according to e.g. the criterion of Kingsburgh & Barlow, 1994). From the VW94 tracks, the nebular age would be 23 000 yrs at the lower mass estimate, and 7 000 yrs at the higher. To convert the progenitor mass range to a main-sequence (MS) age range, we looked at the isochrones of Pietrinferni et al. (2004), for two values of the metallicity $Z = 0.002$ and $Z = 0.008$ ([m/H] = -1 and -0.4 , respectively).

The lower mass value is just below the minimum isochrone mass (0.77 M_{\odot}), so the star might be as old as the Universe. To convert the higher mass value into an age, one needs to decide between canonical core convection, or convection with overshooting, which yields larger ages. In the case of canonical convection, one obtains 2.0 or 2.7 Gyr for the two metallicities, while tracks with overshooting give 3.3 and 4.0 Gyr, respectively. Thus the overall permitted age range is greater than 2 Gyr.

As discussed below, it is also quite possible that the metallicity given by Ar (and S) is closer to the real PN value. In that case, if we take the model argon abundance, then [m/H] = -1.03 ± 0.1 , and by repeating the exercise above, the resulting mass range is 0.70–1.04 M_{\odot} . Taking only isochrones at $Z = 0.002$, the mass interval is then converted into an age interval from 4.7 Gyr to the age of the Universe.

5. Discussion

5.1. Oxygen as a metallicity tracer?

The gas-phase elemental abundance in nebulae which is the easiest to compare to stellar values is that of oxygen (i.e. [O/H]); [O III] lines are collectively strong and usually contain most of the flux from oxygen ions (except in cases of extremely metal-poor nebulae), and thus measurement and abundance-

determination errors are small. Along with sulphur, argon and neon, oxygen is generally considered to be unaffected by endogenous processes within the progenitor stars. For instance, when comparing the oxygen abundances in PNe to those of H II regions in a given galaxy the former are expected to be always lower (or equal) than the latter; H II regions after all represent the present-day metallicity of the ISM, whereas PNe originate from older stellar populations when galactic metallicities are likely to have been smaller. But this is not always found to be the case.

A number of studies of PNe in low-metallicity environments have pointed to a possible enhancement of O/H ascribed to ‘self-enrichment’ processes occurring during the 3rd dredge-up phase. PN vs. H II region abundance comparisons reveal a positive difference between the two at low O/H values (at about $\log O/H < -4$; see e.g. Peña et al. 2007; Richer & McCall 2007). For NGC 3109 (Peña 2007) this is about 0.3 dex, and Kniazev et al. (2007) adopted a similar value of 0.27 dex to ‘correct’ their PN oxygen abundance for ‘self-enrichment’. Comparison between models and observations of PNe in the Magellanic Clouds (Leisy & Dennefeld 2006) have also suggested that oxygen in PNe can be enhanced relative to the precursor metallicities, particularly for the lower mass progenitors. These studies have indicated that argon or sulphur should be used instead of oxygen, as an indicator of the metallicity of the ISM from which the PNe formed, with argon preferred as having the more secure spectral determination; Péquignot et al. (2000) and Péquignot & Tsamis (2005) reached similar conclusions.

It is uncertain whether Benu is likely to contain endogenous oxygen as there are no H II regions in Phoenix to compare to. Its O/H is however higher (by > 0.3 dex) than the range of values found in those PNe for which an oxygen enhancement has been suggested (although see Zijlstra et al. 2006). In addition, following Kniazev et al. (2007) and based on the nebula’s Ne/O, S/O and Ar/O ratios, we should apply no correction for the presence of endogenous oxygen. However, the [Ar/H] abundance is lower than [O/H], so if we adopted the former as an indicator of the metallicity of the parent ISM, as suggested by Leisy & Dennefeld, then we should indeed conclude that endogenous oxygen is present in the nebula. Since with our present knowledge we have no exact way to decide upon this issue, in the rest of the discussion we will adopt a metallicity for the Phoenix galaxy within the range given by [O/H] and [Ar/H], and with the understanding that the more metal-poor end is favoured.

5.2. The age–metallicity relation of Phoenix

In the previous sections we concluded that the spectral properties of the newly discovered PN in Phoenix are consistent with a progenitor mass of $1.0 \pm 0.3 M_{\odot}$ and a metallicity $[m/H] = -0.75 \pm 0.29$ dex (or $Z = 0.002$ to $Z = 0.008$), corresponding to an age of 7.9 ± 5.9 Gyr. Or if argon and sulfur abundances are favored over oxygen, then the progenitor mass and age range are $0.87 \pm 0.17 M_{\odot}$ and 9.2 ± 4.5 Gyr, for $[m/H] = -1.03 \pm 0.1$.

Since this is the first direct spectroscopic determination of this galaxy’s metallicity, it also represents the first solid constraint to its age–metallicity relation (AMR). It is therefore interesting to see how this fits within our present knowledge of the chemical evolution of Phoenix and its star-formation history (SFH).

The evidence accumulated since its discovery by Schuster & West (1976) and its recognition as a dwarf galaxy by Canterna & Flower (1977), clearly shows that Phoenix has had an extended star formation. The presence of an old, globular-cluster like pop-

ulation in Phoenix was first established by the discovery of an extended horizontal branch (HB) at $V \sim 23.8$ (H99; M99). The metallicity of the intermediate–old populations was estimated from the color of the RGB by van de Rydt et al. (1991) and H99, as $[Fe/H] = -2.0$ dex and $[Fe/H] = -1.81 \pm 0.10$ dex, respectively. A significant spread in RGB color was also found which, if it was only due to a metallicity range, would correspond to a dispersion of about 0.5 dex. A very low metallicity at an age of ~ 13 Gyr is then the first point in the AMR of Phoenix.

A number of stars above the RGB tip were interpreted as AGB stars by H99. They are representatives of an intermediate age population (3 to 10 Gyr), which was estimated to be about 30–40% of the total stellar population of the galaxy. The metallicity of these stars could not be estimated, but given the RGB width, it could be even up to -0.3 dex, if we adopted an upper limit of 3σ (i.e. $-1.8 + 3 \times 0.5$ dex).

The presence of a young stellar population was established quite early (Canterna & Flower 1977; Ortolani & Gratton 1988), and together with the possible association of an H I cloud, lead to a morphological classification for the Phoenix as intermediate between dSph and dIrr galaxies (e.g., Young et al. 2007; Carignan, Demers, & Côté, 1991). According to H99 the star formation episode started at least 0.6 Gyr ago, and lasted until 10^8 yr ago. Since the galaxy has no H II regions, and since its main-sequence stars are too faint, no spectroscopic determination exists for the current metallicity of Phoenix.

The current metallicity and future evolution of Phoenix depend on the presence of gas associated with the galaxy. The recent measurement of the optical radial velocity of Phoenix (Irwin & Tolstoy 2002) has shown that it is the same as that of ‘cloud A’ of Young and Lo (1997), confirming a long-suspected association (St-Germain et al. 1999). This means that the H I mass is $\sim 10^5 M_{\odot}$, and as shown in H99, it can be explained by mass lost from RGB and AGB stars, and PNe, over the last ~ 2 Gyr. And according to Young et al. (2007) the gas will not be able to escape the galaxy, so SF might start again in the future. However currently SF from molecular gas is inhibited, since no CO was detected by Buyle et al. (2006), and Jackson et al. (2006) found no diffuse $8 \mu m$ emission from dust. The (unknown) metallicity of Phoenix youngest stars therefore represents the present end point of the galaxy’s chemical evolution.

It is also important to note that age gradients exist throughout the galaxy, with all young stars concentrated in an inner component, while the old population is more extended and oriented N–S (M99; H99). The fraction of intermediate-age stars over old stars also decreases going from the central to the outer regions (Hidalgo et al. 2007). Moreover, additional support for an extended SFH is given by the study of the variable-star content of Gallart et al. (2004). They find both anomalous Cepheids and short-period classical Cepheids, which can be explained if the metallicity has been low ($[Fe/H] = -1.3$) for most of the galaxy’s lifetime.

The star formation history for the central part of Phoenix has been derived by Holtzman et al. (2000; H00) and Young et al. (2007), using a WFPC2 CMD reaching the oldest main sequence turnoffs. Hidalgo et al. (2007) present a determination of both the star formation rate as a function of time (SFR(t)) and the metallicity as a function of time (Z(t)) for the same field and an outer one. All these authors agree on that Phoenix has had an almost continuous SFH, and with a roughly constant star formation rate, somewhat decreasing toward the present time. The star formation rate at intermediate ages ($\simeq 6$ – 2 Gyr) seems to have been somewhat larger than immediately before and after, specially in the central part of the galaxy where Benu resides.

Integrating their age distribution one gets that 15% of the stars have ages between 1.5 and 3 Gyr, and another 15% have ages between 3 and 10 Gyr, which is consistent with the fraction of intermediate-age stars estimated by H99 (see above). Although H00 do not give a real AMR, from their ‘population box’ one can see that the $[\text{Fe}/\text{H}]$ increases from ~ -2 at the earliest stage up to $-(1.5-1)$ at ~ 3 Gyr, then reaches $\sim -1-0$ at ~ 1 Gyr and stays constant thereafter. In the case of H07, they predict quite low metallicities up to the current epoch. The maximum is reached ca. 1 Gyr ago, and it is less than -1 in $[\text{m}/\text{H}]$.

Turning now back to Bennu, we can place its representative point in the AMR relations of H00 and H07, which are the only two studies making quantitative derivations. In the age range of Bennu’s progenitor, most of the simulated stars of H00 have metallicities around $[\text{m}/\text{H}] \sim -1$, but there is also a smaller group of objects with metallicities centered around $[\text{m}/\text{H}] = -0.5$. Adopting instead the age range suggested by argon and sulfur abundances, the metallicities of H00 are around $[\text{m}/\text{H}] \sim -1.5$ with a tail up to $[\text{m}/\text{H}] = -1$. Therefore the metallicity we measure tends to be higher than that of H00 in the same age range, but still compatible within the uncertainties. A metallicity lower than ours is also predicted by the simulations of H07, whose AMR generally stays more metal-poor than that of H00. As it was recalled above, even the peak of the relation happens at a metallicity lower than that of the PN. While an independent study would be needed to resolve this issue, we can conclude that existing AMRs predict, for the age of Bennu, a metallicity that is lower than the one we measure, particularly so for the H07 study.

5.3. Phoenix in the context of Local Group galaxies

5.3.1. The number–luminosity relation

A recent review of the PN population in Local Group (LG) galaxies can be found in Corradi & Magrini (2006; CM06), where they list 20 galaxies containing at least 1 nebula. These objects belong mostly to the northern sky, where the most systematic searches are on-going. There is a very good linear correlation between the V luminosity of a galaxy and the number of PN candidates, which predicts that below $L_V = 10^7 L_\odot$ the probability of finding a PN is very low. This means that in principle Phoenix, which has a $L_V \approx 10^6 L_\odot$, should have no PNe. However the number of nebulae also depends on the SFH of a galaxy, and in particular an enhancement at intermediate ages can also increase the number of detected PNe (see Buzzoni et al. 2006 for a thorough treatment of the luminosity-specific frequency of PNe). Some evidence of this possibility is given in CM06, where it is shown that galaxies with enhanced SFH in the age interval 2 to 8 Gyr have indeed a larger number of PNe (for example NGC 205 and the SMC). The presence of a PN in Phoenix despite its low luminosity could therefore be a sign of substantial SFH at intermediate ages. This is nicely consistent with the large number of AGB stars detected by H99, who, as recalled above, estimated that $\sim 37 \pm 12\%$ of the total population should consist of stars with ages of 3 to 10 Gyr. The enhanced SFR between 2 and 3 Gyr found by H00 (for a central field very close to Bennu) is also in line with this finding. An additional possibility, discussed in the next section, is that the luminosity of Phoenix is underestimated, either because of measurement uncertainties, or because of mass being stripped from the galaxy by the tidal field of the Milky Way. A combination of these two effects might be able to produce a luminosity which is

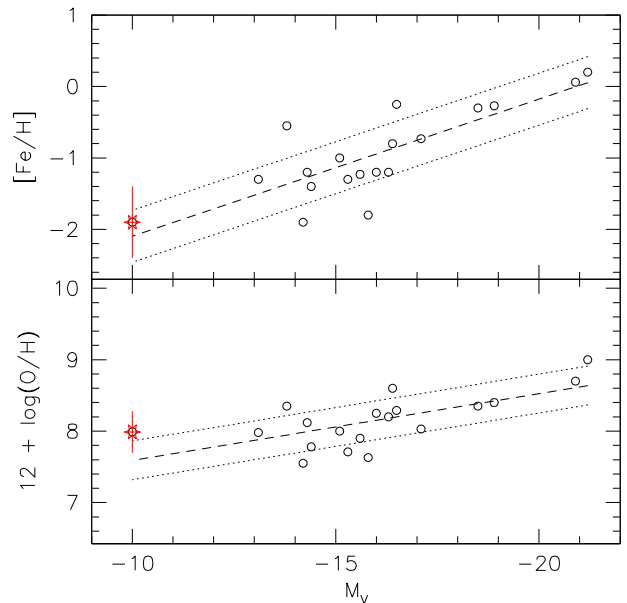


Figure 5. The luminosity-metallicity relation for Local Group galaxies, with data from Corradi (priv. comm.); the $[\text{Fe}/\text{H}]$ values come from stellar results (old–intermediate populations) and $[\text{O}/\text{H}]$ is from nebular abundances (PNe and H II regions; intermediate–young populations). M_V were taken from Mateo (1998). The dashed line represents an unweighted linear fit, while the dotted lines represent the $\pm 1\sigma$ dispersion around the average line.

a factor of 10 larger than what is currently published, and so to reconcile Phoenix with the number–luminosity relation.

5.3.2. The luminosity-metallicity relation

In Fig. 5 we plot the iron and oxygen abundances vs. the absolute V luminosity for a sample of Local Group galaxies (R. Corradi, priv. comm.). The asterisk represents Phoenix, with $[\text{Fe}/\text{H}]$ from H99 and $12 + \log(\text{O}/\text{H})$ from this paper. Its error bars are the 1-sigma dispersion for the iron abundance given by the spread in color of the RGB, while for the oxygen abundance the bar represents our permitted range. The luminosity has been computed by taking the apparent luminosity $V = 13.2$ from de Vaucouleurs & Longo (1988) and converting it into $M_V = -10 \pm 0.13$ with the distance modulus of H99 based on the HB luminosity: $(m - M)_0 = 23.21 \pm 0.08$. An error of 0.1 mag was assumed for the catalog luminosity. Since the relation is steeper for $[\text{Fe}/\text{H}]$, the figure might be telling us that lower-mass galaxies undergo a comparatively larger metal enrichment than higher-mass galaxies, when going from intermediate–old populations to younger populations (note that the range of the y-axis is the same in both panels). In a simple closed-box picture of chemical evolution, this would mean that smaller galaxies have been able to convert larger fractions of their gas into stars. However the figure might also be telling us that $[\text{O}/\text{Fe}]$ is enhanced in low-mass galaxies, as discussed in Sect. 5.1. The scatter of the relations is probably due to a combination of measurement errors, intrinsic abundance scatter, and age differences of the metallicity tracers. Indeed old to intermediate stars contribute to the $[\text{Fe}/\text{H}]$ values estimated

with the color of the RGB, and intermediate to young populations contribute to the [O/H] values from PNe and H II regions.

Figure 5 shows that the value of [O/H] of Phoenix is more than 1-sigma above the average, for its luminosity. There are several possible explanations for this fact. First, it is possible that the PN's oxygen abundance would lead us to overestimate, as discussed in Sect. 5.1, the metallicity of the galaxy. Indeed recent theoretical AGB models by Marigo (2001; M01) predict positive oxygen yields for $0.8 \lesssim M/M_{\odot} \lesssim 3.5$, with a strong dependence on metallicity. This is due to the fact that, as metallicity decreases, the thermal-pulse AGB phase increases its duration. Therefore it allows more dredge-up episodes, which also happen to be more efficient. As we found above, the progenitor star of Benu is in the range $1 \lesssim M/M_{\odot} \lesssim 1.6$ and so it is formally in the range where oxygen enhancement is expected. However in M01 models the yield has a maximum for masses between $2 M_{\odot}$ and $3 M_{\odot}$ and it becomes very modest below $\sim 1.3 M_{\odot}$. On the other hand the minimum metallicity in M01 models is [m/H] = -0.7, and we might expect a larger oxygen enhancement if the metallicity of Benu is closer to -1 as suggested by the argon abundance. Lacking a custom theoretical model constructed for the Phoenix PN progenitor, the conclusion is that an endogenous production of oxygen might explain the position of Phoenix in the luminosity-metallicity relation (see also Magrini et al. 2005 for an extensive discussion of oxygen enhancement in PNe). Note also that, taking argon as a metallicity indicator (i.e. the lowest point of the error bar in the figure), the abundance would be within the r.m.s. dispersion of the relation.

It is also possible that the progenitor was born within an ISM recently enriched by Type II SNe. But perhaps the problem lies in the luminosity of the galaxy. The *V* luminosity is flagged as 'Low quality data' in the *NASA/IPAC Extragalactic Database*, and for example the *R* luminosity from Lauberts and Valentijn (1989) is 1 magnitude brighter. A luminosity of ~ -11 would bring the galaxy within the 1-sigma dispersion of the relation. And finally another possibility is that the current mass of the galaxy is not representative of the mass at the time when the PN was born. In fact M99 find that the radial profile of Phoenix can be well fit by a King model, which suggests a tidal truncation by the gravitational field of the Milky Way. It also means that part of the galaxy mass was lost due to dynamical evolution, and hence that the luminosity of Phoenix was larger in the past.

6. Summary and conclusions

A planetary nebula was recently discovered in the Phoenix dwarf galaxy, the first ever found in this stellar system. In this paper we presented our follow-up spectroscopic data obtained at the ESO/VLT with FORS1. With a total exposure time of 1.4 hours we measured emission line fluxes down to 9×10^{-19} erg cm $^{-2}$ s $^{-1}$. Such high sensitivity allowed to detect, together with the Balmer series, all lines of oxygen, neon, sulfur, helium, argon, and nitrogen above the quoted threshold. To calculate the abundances of these elements, both the empirical method, and photoionization modeling were employed. The element-to-hydrogen abundance ratios were found to be consistent with each other for the two methods, but the second method yields more reasonable luminosity and temperature for the central star. The oxygen abundance is larger than that of argon and sulfur. This might be due to endogenous production of oxygen in the progenitor, or it might be caused by a truly higher oxygen abundance of the ISM where the progenitor was born. To decide between the two hypotheses an independent measurement of the abundance would be needed, which however does not exist. Therefore we based our discus-

sion on a metallicity range comprised between [m/H] = -1.03 (sulfur and argon abundances) and [m/H] = -0.46 (oxygen abundance). Our conclusions would be essentially the same if we restricted the metallicity range to that allowed by argon and sulfur alone.

Using VW04 tracks and Pietrinferni et al. (2004) isochrones, we found that the progenitor star of Benu should have an age comprised between 2.0 and 13.7 Gyr. The more restrictive low metallicity would give an age 9.2 ± 4.5 Gyr. So despite a considerable uncertainty, the Phoenix PN allows to put a constrain on the galaxy's age-metallicity relation. This shows that existing AMRs underestimate the metallicity at intermediate ages, by as much as ~ 0.6 dex, even when adopting the most restricted [m/H] range.

Within the general picture of LG dwarf galaxies, the presence of a PN in Phoenix is unexpected given the galaxy's low luminosity (Corradi & Magrini 2006). Moreover, an extrapolation of a linear L-Z relation to the luminosity of Phoenix would suggest that the metallicity of the galaxy is larger than that of other LG galaxies of comparable luminosity (at an intermediate age). On the other hand there are no other galaxies at such low luminosity with measured nebular oxygen abundance, so it might be possible that the relation simply deviates from linearity for the lowest-mass galaxies. Another possibility is that the problem resides in the luminosity. The galaxy might be more luminous than quoted in the literature, so a modern measurement of the integrated light would be very desirable. It is also very likely that Phoenix lost a fraction of its mass through tidal interaction with the gravitational potential of the Milky Way (M99), so its representative point in the L-Z relation should be moved to higher values of L. This would also help with the PN-number vs. luminosity relation, thereby explaining the presence of Benu.

In conclusion, this work demonstrates that the detection of even a single PN in a dwarf galaxy, can provide essential information on its chemical and dynamical evolution, and it can lead to a better understanding of its past star formation history and mass build-up.

Acknowledgements. David Martínez-Delgado-Delgado identified the candidate PN during run 63.I-0642 by blinking the *V* and *R* images. This research has made use of the *NASA/IPAC Extragalactic Database* (NED) which is operated by the Jet Propulsion Laboratory, California Institute of Technology, under contract with the National Aeronautics and Space Administration. We thank the referee Romano Corradi for a meticulous examination of our paper which lead to a substantially improved manuscript.

References

- Allende-Prieto, C., Lambert, D. L., & Asplund, M. 2001, *ApJ*, 556, 63
- Asplund, M., Grevesse, N., & Sauval, A. J. 2005, *ASPC*, 336, 25
- Benjamin, R. A., Skillman, E. D., & Smits, D. P. 1999, *ApJ*, 514, 307
- Buyle, P., Michielsen, D., de Rijcke, S., Ott, J., & Dejonghe, H. 2006, *MNRAS*, 373, 793
- Buzzoni, A., Arnaboldi, M., & Corradi, R. L. M. 2006, *MNRAS*, 368, 877
- Canterna, R., & Flower, P. J. 1977, *ApJ*, 212, L57
- Carignan, C., Demers, S., & Côté, S. 1991, *ApJ*, 381, L13
- Clegg, R. E. S., Harrington, J. P., Barlow, M. J., & Walsh, J. R. 1987, *ApJ*, 314, 551
- Corradi, R. L. M., & Magrini, L. 2006, in *Planetary nebulae beyond the Milky Way*, eds Stanghellini, L., Walsh, J. R., & Douglas, N. G., Springer, Berlin p.36
- de Vaucouleurs, A., & Longo, G. 1988, *Catalogue of visual and infrared photometry of galaxies from 0.5 micrometer to 10 micrometer (1961-1985)*, University of Texas Monographs in Astronomy
- Dudziak, G., Péquignot, D., Zijlstra, A. A., & Walsh, J. R. 2000, *A&A*, 363, 717
- Exter, K. M., Barlow, M. J., & Walton, N. A. 2004, *MNRAS*, 349, 1291
- Gallart, C., Martínez-Delgado, D., Gómez-Flechoso, M. A., & Mateo, M. 2001, *AJ*, 121, 2572

- Gallart, C., Aparicio, A., Freedman, W. L., Madore, B. F., Martínez-Delgado-Delgado, D., & Stetson, P. B. 2004, *AJ*, 127, 1486
- Hamuy, M., Suntzeff, N. B., Heathcote, S. R., Walker, A. R., Gigoux, P., & Phillips, M. M. 1994, *PASP*, 106, 566
- Held, E. V., Saviane, I., & Momany, Y. 1999, *A&A*, 345, 747 (H99)
- Hidalgo, S. L., Aparicio, A., & Martínez-Delgado, D. 2007, in preparation
- Holtzman, J. A., Smith, G. H., & Grillmair, L. 2000, *AJ*, 120, 3060
- Howarth, I. D., Murray, J., Mills, D., & Berry S. 1998, *Starlink User Note* 50.12
- Irwin, M., & Tolstoy, E. 2002, *MNRAS*, 336, 643
- Jackson, D. C., et al. 2006, *ApJ*, 646, 192
- Kaler, J. B., & Jacoby, G. H. 1989, *ApJ*, 345, 871
- Kingsburgh, R. L., & Barlow, M. J. 1994, *MNRAS*, 271, 257
- Kniazev, A. Y., Grebel, E. K., Pustilnki, S. A., & Pramskij, A. G. 2007, *A&A*, 468, 121
- Lauberts, A., & Valentijn, E. A. 1989, *The Surface Photometry Catalogue Of The ESO-Uppsala Galaxies*, ESO, Garching Bei Munchen
- Leisy, P., & Dennefeld, M. 2006, *A&A*, 456, 451
- Lodders, K. 2003, *ApJ*, 591, 1220
- Magrini, L., Leisy, P., Corradi, R. L. M., Perinotto, M., Mampaso, A., Vilchez, J. M., 2005, *A&A*, 443, 115
- Marigo, P., 2001, *A&A*, 370, 194
- Martínez-Delgado, D., Gallart, C., & Aparicio, A. 1999, *AJ*, 118, 862 (M99)
- Mateo, M. 1998, *ARA&A*, 36, 435.
- Ortolani, S., & Gratton, R. G. 1988, *PASP*, 100, 1405
- Peña, M., Richer, M., & Stasińska, G. 2007, *RMxAC*, 29, 83
- Péquignot, D., Walsh, J. R., Zijlstra, A. A., & Dudziak, G. 2000, *A&A*, 361, L1
- Péquignot, D., & Tsamis, Y.G. 2005, *A&A*, 430, 187
- Pietrinferni, A., Cassisi, S., Salaris, M., & Castelli, F. 2004, *ApJ*, 612, 168
- Pont, F., Zinn, R., Gallart, C., Hardy, E., & Winnick, R. 2004, *AJ*, 127, 840
- Rauch, T. 2003, *A&A*, 403, 709
- Richer, M. G., & McCall, M. L. 2007, *ApJ*, 658, 328
- Schuster, H.-E., & West, R. M. 1976, *A&A*, 49, 129
- Shields, G. A. 2002, *RMxAC*, 12, 189
- Smits, D. P. 1996, *MNRAS*, 278, 683
- Stasińska, G., & Izotov, Y. 2003, *A&A*, 397, 71
- St-Germain, J., Carignan, C., Côte, S., & Oosterloo, T. 1999, *AJ*, 118, 1235
- Storey, P. J., & Hummer, D. G. 1995, *MNRAS*, 272, 41
- Stoy, R. H. 1933, *MNRAS*, 93, 588
- van de Rydt F., Demers S., & Kunkel W. W. 1991, *AJ* 102, 130
- Vassiliadis, E., & Wood, P. R. 1994, *ApJS*, 92, 125
- Young, L. M., & Lo, K. Y. 1997, *ApJ*, 490, 710
- Young, L.M., Skillman, E.D., Weisz, D.R. & Dolphin, A.E. 2007, *ApJ*, 659, 331
- Zanstra, H. 1927, *ApJ*, 65, 50
- Zijlstra, A. A., & Pottasch, S. R. 1989, *A&A*, 216, 245
- Zijlstra, A., Gesicki, K., Walsh, J. R., Péquignot, D., van Hoof, P. A. M., & Minniti, D. 2006, *MNRAS*, 369, 875

Appendix A: Photoionization model outputs

Two-sector models ('D') using standard assumptions (Table 4) and one-sector models ('S'), labelled by T_{BB} in kK, are presented in Table A.1. All but one (D135) fall outside the domain where 'exact' solutions can be found (Sect. 4.2, Table 5), and 'best fit' values are adopted for He I, [Ar III], [Ar IV] and even He II. D105 cannot account for He II for any He/H and τ_1 , and the computed He I is unacceptably large. D160 illustrates the maximum T_{BB} obtained when the computed He I $\lambda 5876$ intensity is allowed to depart from observation by at most 33%. For even larger T_{BB} , He I is underestimated and the ratio [Ar IV]/[Ar III] is not accounted for either. Also, the optically thick sector can develop a warm neutral zone beyond the ionization front that emits (unobserved) [O I] $\lambda 6300$.

Computed [S II] and [S III] intensities for D135 suggest that S/Ar may be up to twice larger than the adopted solar value, but this is not judged significant, given the weakness of observed [S III] $\lambda 6312$. From the strongest predicted iron line, [Fe VI] $\lambda 5145$, an upper limit to Fe/H is twice the adopted value, so that Fe/Ar is less than 0.25 solar: as in usual PNe, most of the iron is likely to be locked into dust grains. In Table A.1, the ratio [Ar IV] $\lambda 4711$ +/[Ar IV] $\lambda 4740$ increases with T_{BB} due to the growing contribution of [Ne IV].

For single-sector uniformly matter-bounded models to simultaneously account for He II and [O II] requires, at the same time, a high T_{BB} , a low L and small ionization parameter (large R_{in} and/or large N_{in}). These models typically fail to reproduce the argon ionization balance, underestimating the [Ar IV]/[Ar III] ratio by factors of $\gtrsim 3$, and imply large He/H (in the models displayed, He/H is too small). These models are rejected, as well as their low value of O/H. Any positive detection of [O I] would further invalidate the single-sector assumption.

Appendix B: The central star parameters

Uncertainties affecting the model geometry and the spectroscopic constraints can enlarge the domain of acceptable solutions in the (T_{BB} , L) plane. Uncertainties on L , related to R_{in} and to [Ar IV]/[Ar III], amount to a factor of 1.6 and are therefore not too influential in the interpretation of the stellar parameters (Sect. 5). This factor, obtained assuming a factor 1.45 uncertainty on [Ar IV]/[Ar III], allows for both observational and theoretical uncertainties (the recombination coefficients for argon are inaccurate, e.g., Dudziak et al. 2000). The range of accessible T_{BB} is controlled by the assumed value of $N_{\text{in}}(\text{H})$ (Table 5) and, particularly, the intensity of He I $\lambda 5876$. The computed He I increases rapidly towards low values of T_{BB} (alias T_{eff}) because He/H must increase to account for He II (see model D105, Col. 2 of Table A.1). In addition, the assumption of a strict black body for the central star, useful in accounting for the strong He II line, is more likely to break down for lower T_{eff} 's due to the occurrence of a discontinuity at the ionization limit of He⁺ (e.g., Rauch 2003), thus exacerbating the problem. By itself, the increase of He/H strongly militates against too small values of T_{BB} . Thus, a lower limit to T_{BB} is likely close to 120 kK, corresponding to a minimum $T_{\text{eff}} \sim 105$ kK (Eq. 2). On the other hand, trial computations showed that dividing the present He I line intensity by 1.33, models could be obtained up to $T_{\text{BB}} = 160$ kK (D160, Col. 4 of Table A.1), equivalent to a maximum $T_{\text{eff}} \sim 145$ kK. In fact, a few models re-converged using stellar atmosphere models (Rauch 2003; see Fig. 22 in Péquignot & Tsamis 2005) showing that a more nearly correct maximum T_{eff} is almost 150 kK. More accurate He I line intensities are needed before the range of possible T_{eff} 's can be narrowed. Note that the derived standard He/H (= 0.108) is relatively large, suggesting that either the observed He II line intensity is slightly overestimated or some basic model assumption is lacking. To our knowledge, only in a situation of chemical inhomogeneity of the PN could the derived He/H be lowered (Péquignot et al. 2002). Indications in favour of such a possibility are: (i) H γ is observed to be stronger than expected, and (ii) the [S II]+C III $\lambda 4069$ and C IV+[Fe III] $\lambda 4658$ blends are severely underestimated in all models (Table A.1). These spectral regions include C and O recombination multiplets which in many PNe can only be accounted for with models that harbour H-deficient inclusions (Péquignot et al. 2002). The current observations of Bennu are not sufficiently deep to allow us to pursue this possibility further.

Table A.1. Model parameters and results.

Model ^a	D105	D135	D160	S180	S310	
L (L_{\odot})	2423	2550	2420	2080	2084	
R_{in} (10^{17} cm)	1.00	1.00	1.00	2.58	1.82	
$R_{\text{out}}(\text{thin})$ (10^{17} cm)	2.08	2.15	2.14	2.97	2.06	
$R_{\text{out}}(\text{thick})$ (10^{17} cm)	2.91	2.98	2.80	—	—	
$f^{\text{cov}}(\text{thick})$	0.027	0.013	0.012	—	—	
$N_{\text{in}}(\text{H})$ (cm^{-3})	1200	1200	1200	1000	1600	
$\langle n_e \rangle$ (cm^{-3})	1942	1860	1870	1590	2940	
$\langle T(\text{H}^+) \rangle$ (10^4 K)	1.752	1.780	1.781	1.730	1.669	
τ_{c}	1.00	1.75	1.65	0.90	0.90	
$\tau(\text{thin})$ (13.6 eV)	0.50	0.79	1.09	1.37	3.40	
H β (thin) fraction	0.73	0.87	0.89	1.00	1.00	
M_{ion} ($10^{-2} M_{\odot}$)	6.83	7.02	6.85	6.11	3.37	
He/H	0.122	0.108	0.105	0.120	0.110	
C/H ($\times 10^{-5}$)	13.0	22.0	26.5	11.7	25.0	
N/H ($\times 10^{-5}$)	1.30	2.56	3.10	1.42	1.24	
O/H ($\times 10^{-5}$)	8.35	17.5	22.0	7.72	8.26	
Ne/H ($\times 10^{-5}$)	1.22	2.57	3.49	1.29	1.50	
S/H ($\times 10^{-7}$)	14.9	17.3	19.7	12.7	11.4	
Ar/H ($\times 10^{-7}$)	3.40	3.96	4.55	2.90	2.60	
Fe/H ($\times 10^{-7}$)	4.00	4.00	4.00	4.00	4.00	
<i>Lines</i>	I_{obs}^b	<i>Predicted intensity / Observed intensity</i>				
H α 6563	284.	0.99	0.99	1.00	1.04	1.06
H γ 4340	50.4	0.94	0.94	0.94	0.94	0.94
H δ 4101	27.7	0.96	0.97	0.97	1.00	1.01
He I 5876	2.8	2.56	1.00	0.75	1.13	0.74
He II 4686	98.1	0.88	1.00	1.00	0.98	0.91
C III] 1908	—	(591)	(573)	(582)	(625)	(1267)
C IV 1549	—	(1239)	(1864)	(1978)	(667)	(835)
C IV 4658 ^c	3.0:	0.12	0.18	0.22	0.12	0.09
[N II] 6584	9.4	1.00	1.00	1.00	1.00	1.00
[O I] 6300	<2.	0.64	0.74	0.77	0.03	0.03
[O II] 3727	26.8	1.00	1.00	1.00	1.00	1.00
[O III] 4363	8.3	1.00	1.00	1.00	1.00	1.00
[O III] 5007+	451.	1.00	1.00	1.00	1.00	1.00
[O IV] 26 μm	—	(229)	(551)	(619)	(151)	(107)
[Ne III] 3868	28.0	1.00	1.00	1.00	1.00	1.00
[S II] 4069 ^c	3.7:	0.31	0.22	0.24	0.25	0.21
[S II] 6716	1.7:	0.60	0.40	0.39	0.50	0.41
[S II] 6731	2.6:	0.63	0.41	0.40	0.49	0.41
[S III] 6312	1.1:	0.94	0.71	0.74	1.29	1.11
[Ar III] 7136	2.7	1.38	1.00	1.00	1.63	1.45
[Ar IV] 4711 ^c	5.4	0.76	0.95	1.02	0.41	0.29
[Ar IV] 4740	2.7	0.93	1.00	1.00	0.47	0.34
[Fe VI] 5145	<3.	0.33	0.48	0.42	0.26	0.20

[^a] D and S refer to 2- and 1-sector models respectively. Models are labelled by T_{BB} in kK.

[^b] ‘<’ upper limit and ‘:’ large uncertainty. Unobserved lines: predicted intensities are given in parentheses in units of H β = 100.

[^c] Blends: C IV 4658 + [Fe III] 4658 + C III 4649 + O II 4651; [S II] 4069 + [Fe V] 4071 + C III 4069; [Ar IV] 4711 + He I 4713 + [Ne IV] 4714+16.